NANO LETTERS
Letter
pubs.acs.org/NanoLett

Multilayer Black Phosphorus as a Versatile Mid-Infrared Electro-optic Material

Charles Lin,*[,†] Roberto Grassi,[‡] Tony Low,[‡] and Amr S. Helmy[†]

[†]The Edward S. Rogers Department of Electrical and Computer Engineering, University of Toronto, 10 King's College Road, Toronto, ON M5S 3G4, Canada

[‡]Department of Electrical and Computer Engineering, University of Minnesota, 200 Union Street SE, 4-174 Keller Hall, Minneapolis, Minnesota 55455-0170, United States

S *Supporting Information*

ABSTRACT: We investigate the electro-optic properties of black phosphorus (BP) thin films for optical modulation in the mid-infrared frequencies. Our calculation indicates that an applied out-of-plane electric field may lead to red-, blue-, or bidirectional shift in BP's absorption edge. This is due to the interplay between the field-induced quantum-confined Franz-Keldysh effect and the Pauli-blocked Burstein−Moss shift. The relative contribution of the two electro-absorption mechanisms depends on doping range, operating wavelength, and BP film thickness. For proof-of concept, simple modulator configuration with BP overlaid over a silicon nanowire is studied. Simulation results show that operating BP in the quantum-confined Franz-Keldysh regime can improve the maximal attainable absorption as well as power efficiency compared to its graphene counterpart.

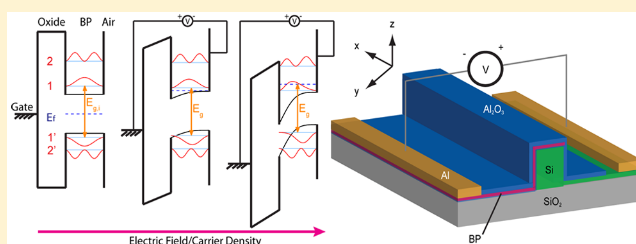

KEYWORDS: *Black phosphorus, electro-optics, quantum-confined Franz-Keldysh effect, Burstein−Moss shift, mid-infrared, modulator*

The mid-infrared (MIR) regime contains the fingerprints of many common molecular vibrations and covers several atmospheric transmission windows, making it important for spectroscopic molecular analysis, sensing, and free-space optical communications.[1,2] As such, integrated photonic solutions that can operate between $\lambda = 2-10$ μm are of great technological importance. In particular, progress has been made in components such as broadband and frequency comb sources with on-chip form-factor,[3,4] Si_3N_4 and SiGe-based low-loss optical waveguides, and photodetectors utilizing low-bandgap materials.[5] However, the realization of MIR optical modulators, which require material platforms with versatile optoelectronic properties, remains challenging.

Materials with superior electro-optic properties for modulation have experienced remarkable developments in the telecommunication spectrum (0.8−1.7 μm). This can be attributed to the advents of bandgap engineering in III−V heterostructures as well as the quantum-confined Stark effect (QCSE), where the absorption band edge of quantum well (QW) shifts toward lower energy in the presence of a transverse electric field.[6−10] With recent focus on utilizing the Si-on-insulator (SOI) platform to implement and integrate all possible optoelectronic functions, numerous developments have been made in using Si/SiGe heterostructures.[11,12] However, as these materials cannot operate beyond the near-IR, materials with suitable physical and optoelectronic properties for optical modulation on SOI is still lacking in the MIR.

Recently, interest in multilayer black phosphorus (BP) thin-film has reemerged.[13−19] In its bulk form, BP is a semiconductor with a direct bandgap of 0.3 eV, and its measured Hall mobilities approaches 10 000 $cm^2/(V\ s)$. In its thin-film form, the optical spectra of multilayer BP varies with thickness as well as light polarization across mid- to near-IR frequencies.[20−23] Similar to graphene, the reduced dimensionality in BP allows the Pauli-blocked Burstein−Moss shift (BMS) to manifest through increased doping.[20,24−28] Recent electrical measurements on multilayer BP showed encouraging results.[13−16,18] Moreover, studies on the BP phototransistor have demonstrated hyperspectral light detection covering both visible and IR frequencies.[18,29] This is followed by the report of a waveguide-integrated multilayer BP photodetector that has intrinsic responsivity of 135 mAW^{-1}.[30] In addition, it showed orders of magnitude reduction in dark current compared to its graphene-counterpart, thereby revealing BP's potential for improving the power-efficiency of optoelectronic components.

In this work, we examine the viability of BP thin-films as electro-optic material for modulation in the MIR frequencies. Our calculations show that, under an applied out-of-plane electric field, the interplay of field-induced quantum-confined Franz-Keldysh (QCFK) effect and carrier-induced BMS leads to versatile optoelectronic attributes: BP's absorption spectra may undergo red-, blue-, or bidirectional shift depending on doping level, wavelength, and BP film thickness. Through simulation of a simple optical modulator with BP overlaid over

Received: November 10, 2015
Revised: February 8, 2016
Published: February 22, 2016

© 2016 American Chemical Society

DOI: 10.1021/acs.nanolett.5b04594
Nano Lett. 2016, 16, 1683−1689

a silicon nanowire, we elucidate BP's potential for improving the maximal attainable absorption and power efficiency compared to its graphene counterpart.

BP has an orthorhombic crystal structure consisting of puckered layers as illustrated in Figure 1a. It exhibits anisotropic in-plane optical properties, with the armchair direction (x) corresponding to the lower in-plane effective mass direction.[17] Moreover, it has a direct gap at Γ point, estimated to be between 2 and 0.3 eV for monolayer and bulk BP, respectively.[17,23,31] In this work, we assume that multilayer BP has the same stacking as that of its bulk parent[32] and note that differently stacked BP can lead to a different behavior due to their varying electronic structures.[33] Cyclotron resonance experiments on bulk BP[34] have found the out-of-plane effective masses to be considerably smaller than that of TMDs[35] and graphite.[36] Adopting an average of experimental[34] and theoretical[20] values, the electron and hole out-of-plane masses are about $m_{cz} = 0.2m_0$ and $m_{vz} = 0.4m_0$, respectively.

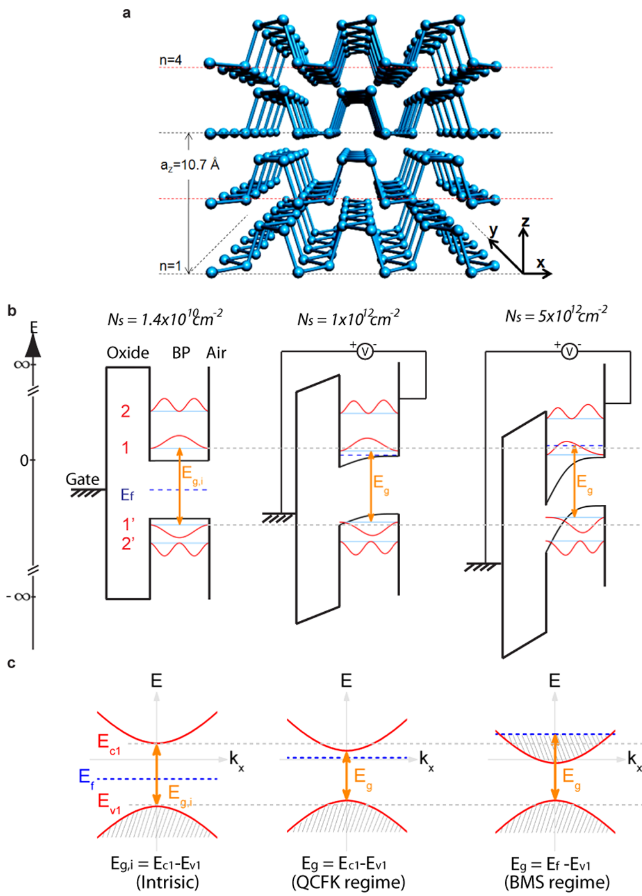

Figure 1. (a) Lattice structure of BP. Layer numbers n are indicated. a_z is the lattice constant in the out-of-plane direction. The thickness of the multilayer BP is then given by $n \times a_z/2$. (b) Schematic, energy band diagram, and wave functions of 5 nm thick BP QW with $N_s = 1.4 \times 10^{10}$ (intrinsic regime), 1×10^{12} (QCFK regime), and 5×10^{12} cm^{-2} (BMS regime). Results are computed through self-consistent Schrödinger-Poisson calculation. The energy zero is chosen to be the at the bottom and center of the conduction band. (c) Energy dispersion diagrams for the lowest/highest conduction/valence subband under doping conditions listed above. The level of carrier occupancy is indicated by the shaded region. The corresponding formula for calculating E_g is also listed.

Here, we examine the electrostatics in a 5 nm BP QW under the presence of an out-of-plane electric field. We model its electronic structure around the Γ point using the $k{\cdot}p$ approximation with a two-band Hamiltonian, as described elsewhere.[20,37] See Methods for detailed description. With an infinite potential barrier assumption, we solved for the QW electrostatics self-consistently.[38] In the intrinsic case, i.e., when the Fermi energy (E_f) is approximately located at midgap, the electron carrier density (N_s) of the 5 nm BP QW is calculated to be 1.4×10^{10} cm^{-2}, albeit compensated by the same amount of hole density. Here, the intrinsic case also corresponds to flatband condition. In this work, we define the optical bandgap, E_g, to be the optical transition energy between the highest filled state in the valence band and the lowest unoccupied state in conduction band. For our intrinsic 5 nm BP film, this is determined to be $E_{g,i} = E_{c1} - E_{v1} = 0.62$ eV, where E_{c1} and E_{v1} are the energy levels of the first conduction and valence subbands, respectively.

Figure 1b presents the energy band diagram of the 5 nm BP QW in the out-of-plane direction. Results are calculated using the effective mass along the armchair direction (x), which corresponds to higher optical conductivity and hence more favorable for optoelectronic applications.[20] With the application of a positive external gate bias, the out-of-plane electric field leads to band-bending across the QW, bringing the electron and hole subbands closer in energy, hence effectively reducing E_g.[6] Such bandgap shrinkage due to Stark shift have been recently observed experimentally in multilayer BP[39] and can be described by the QCFK effect[40] since the excitonic effect is negligible for BP thickness greater than 4 nm.[23,41] Concurrently, the induced N_s leads to the formation of 2D electron gas at the BP-oxide interface and also raises the E_f of the QW. As the electron gas becomes more degenerate, Pauli blocking of the optical transitions lead to broadening of E_g, as described by BMS.[19,42,43] The former mechanism leads to a red-shift, while the latter effect appears as a blue-shift. The dispersion diagrams shown in Figure 1c illustrate these optical processes. The net shift in E_g due to an external bias can therefore be described by

$$\Delta E_g \propto \Delta_{QCFK} + \Delta_{BMS} \tag{1}$$

The bias-induced band-bending has a negative contribution to E_g and can be approximated by

$$\Delta_{QCFK} \sim \Delta(E_{c1} - E_{v1}) \tag{2}$$

The shift in E_g in a degenerate electron gas due to Pauli blocking, ignoring the conduction and valence bands asymmetry, can be approximated by

$$\Delta_{BMS} \sim 2\Delta(E_f - E_{c1})\theta(E_f - E_{c1}) \tag{3}$$

for electron-doped BP, where $\theta(...)$ denotes the heaviside step function. When E_f raises beyond E_{c1}, Δ_{BMS} acquires a positive contribution to E_g. A similar expression holds for the hole-doped case.

We calculate BP's optical conductivity tensor (σ_{ij}) using the Kubo formula within an effective low-energy Hamiltonian as described elsewhere.[20] The temperature is taken to be 300 K in all calculations. Figure 2a displays the real part of the σ_{xx} spectra for a 5 nm BP thin-film under different biasing conditions. The corresponding differential conductivity spectra Re($\sigma_{xx} - \sigma_{xx,i}$) are shown in Figure 2b. Results are normalized with respect to $\sigma_0 = e^2/4\hbar$, the universal conductivity of graphene,[44,45] and the photon energies E are displayed with respect to $E_{g,i}$. We

DOI: 10.1021/acs.nanolett.5b04594
Nano Lett. 2016, 16, 1683−1689

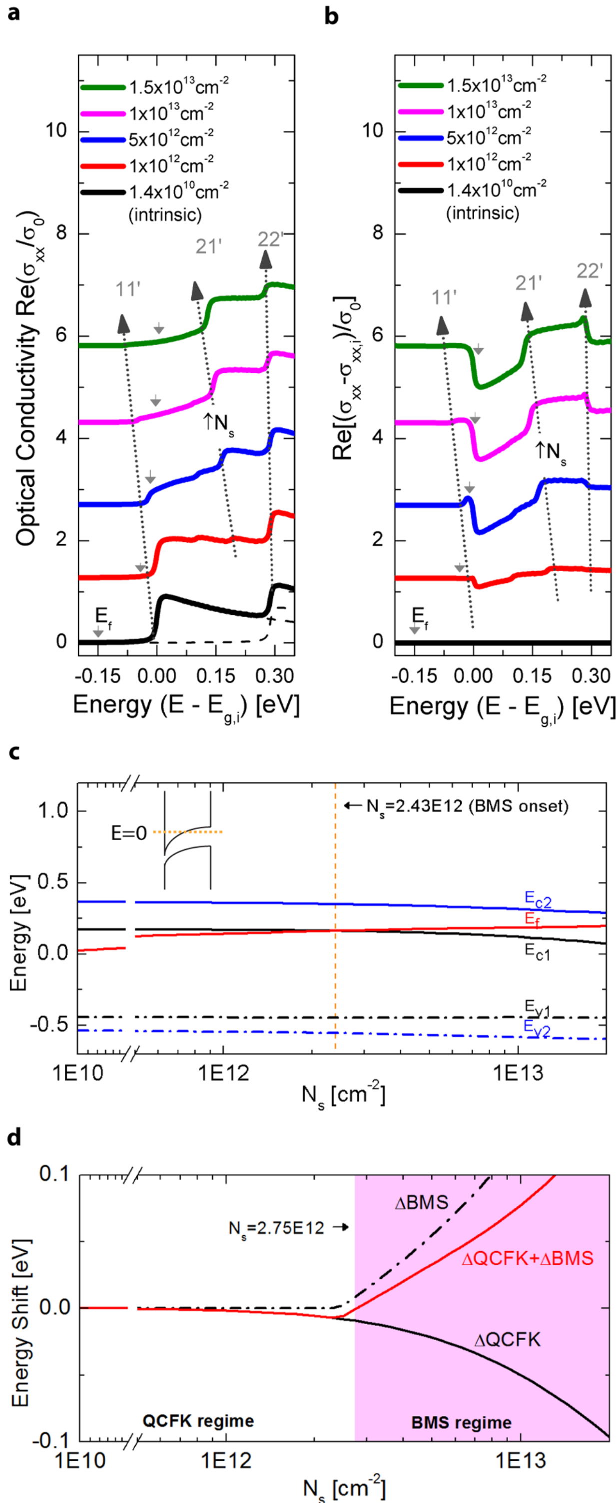

Figure 2. (a) Evolution of σ_{xx} of a 5 nm BP QW due to increasing N_s level. Conductivities and photon energies are normalized with respect to $\sigma_0 = e^2/4h$ and $E_{g,i}$ (0.62 eV), respectively. The intersubband contributions to σ_{xx} are illustrated for intrinsic BP ($N_s = 1.4 \times 10^{10}$ cm^{-2}). (b) Differential conductivity spectra, $(\sigma_{xx} - \sigma_{xx,i})/\sigma_0$, of the 5 nm BP QW. (c,d) Calculated QW energies and shifts in E_g due to QCFK effect and BMS (described by eq 2 and 3, respectively).

consider a range of positive bias, up to carrier concentration of $N_s \sim 1.5 \times 10^{13}$ cm^{-2}, a value routinely obtained in experiments with layered materials. It is observed that BP's σ_{xx} not only shows strong doping dependence similar to that of graphene (see accompanying Supporting Information), but also exhibits oscillatory behavior, which can be traced to the underlying electronic subbands structure. We explain these trends in more detail below, by examining optical transitions between electron and hole subbands across the band gap, i.e., E_{cn} and E_{vm}:

$E_{c1}-E_{v1}$ Transition. For intrinsic BP, the oscillator strength is nonzero only for optical transitions between subbands of the same indices, i.e., $m = n$. Hence, the lowest energy optical transition, $E_{c1}-E_{v1}$, defines the optical bandgap E_g, as apparent in Figure 2a. With increased N_s, the red-shift of the optical spectra is clearly observed. The energy levels of the QW as a function of N_s is displayed in Figure 2c. The energy zero is chosen to be at the center of the conduction band bottom (see inset). The narrowing of E_g as described by QCFK effect is attributed to the effective lowering of E_{c1} and E_{v1}. For progressively higher N_s, hence stronger external field across the QW, the electron and hole wave functions start to shift to opposite sides of the QW (Figure 1b).[6] Consequently, the strength of the transition is reduced and its optical band edge becomes smeared, as reflected in Figure 2a.

$E_{c2}-E_{v1}$ Transition. With sufficient electric field strength, the wave function overlap between $m \neq n$ subbands becomes finite, resulting in the appearance of added "ripples" in σ_{xx} (Figure 2a). The induced tail and the additional oscillatory features below and above $E_{g,i}$ are both characteristics of the QCFK effect.[40] For $N_s > 5 \times 10^{12}$ cm^{-2}, the $E_{c2}-E_{v1}$ transition becomes the dominant feature in the optical spectra. The field-induced red-shift similar to that of $E_{c1}-E_{v1}$ transition is observed, but the absorption edge becomes more abrupt with increased doping, thereby elucidating the contribution from BMS.

$E_{c2}-E_{v2}$ Transition. For this 5 nm BP film, the second subband energies are larger than the band bending of the QW. Moreover, only the E_{c1} subband is populated for the chosen doping range. Thus, the position of this transition remains almost invariant (Figure 2a).

Figure 2d studies the doping-dependence of Δ_{QCFK} and Δ_{BMS} in the 5 nm BP QW. Depending on the doping level, the change in E_g may be categorized into two regimes, each dominated by different electro-absorption mechanisms. For low N_s, the E_f level is lower than E_{c1}, indicating a red-shift of E_g as only Δ_{QCFK} provides finite contribution. At $N_s = 2.43 \times 10^{12}$ cm^{-2}, the E_f and E_{c1} levels crosses, after which Δ_{BMS} increases rapidly, eventually matches and exceeds Δ_{QCFK} at $N_s = 2.75 \times 10^{12}$ cm^{-2}. For high N_s, blue-shift of E_g starts to manifest, albeit counteracted by Δ_{QCFK}. The evolution and transition between the two absorption regimes are further elucidated in the differential conductivity spectra (Figure 2b). For $N_s = 5 \times 10^{12}$ cm^{-2}, the QCFK-induced red-shift in E_g results in an asymmetric line shape, where an increase/decrease of $\Delta\sigma_{xx}$ at photon energies below/above $E_{g,i}$ can still be observed. Conversely, for $N_s = 1 \times 10^{13}$ cm^{-2}, a large decrease of $\Delta\sigma_{xx}$ above $E_{g,i}$, a characteristic of BMS, is obtained.

Other than doping, the optical absorption spectra of BP thin films also vary sensitively with the number of layers. Figure 3a shows the change in E_g as a function of doping, for BP QW with thickness of 4, 7, and 10 nm. The difference between Δ_{BMS} and $|\Delta_{QCFK}|$ for high N_s level reduces with increased thickness as wider QWs have lower subband energies and thus are more strongly influenced by external electric field. The σ_{xx} spectra for the QWs are displayed from Figure 3b–d, where E_g and optical band edge, defined as $0.1 \times \sigma_0$, are also indicated. In general,

DOI: 10.1021/acs.nanolett.5b04594
Nano Lett. 2016, 16, 1683–1689

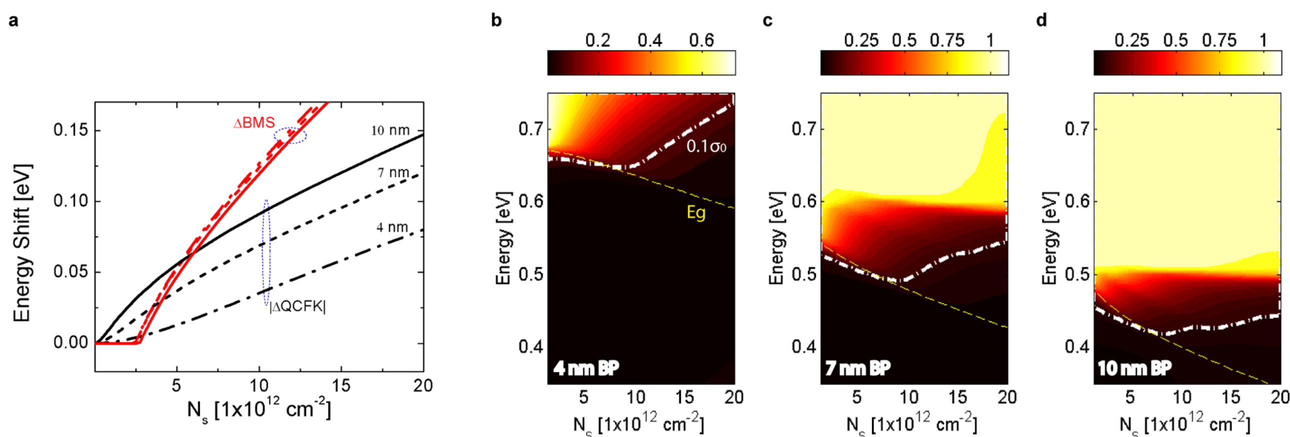

Figure 3. (a) Calculated shift in E_g due to Δ_{BMS} and Δ_{QCFK} for 4, 7, and 10 nm BP QWs, plotted as a function of N_s. (b–d) Optical conductivities (σ_{xx}) of the respective QWs, plotted as a function of N_s and photon energy (E). Conductivities are normalized with respect to $\sigma_0 = e^2/4h$.

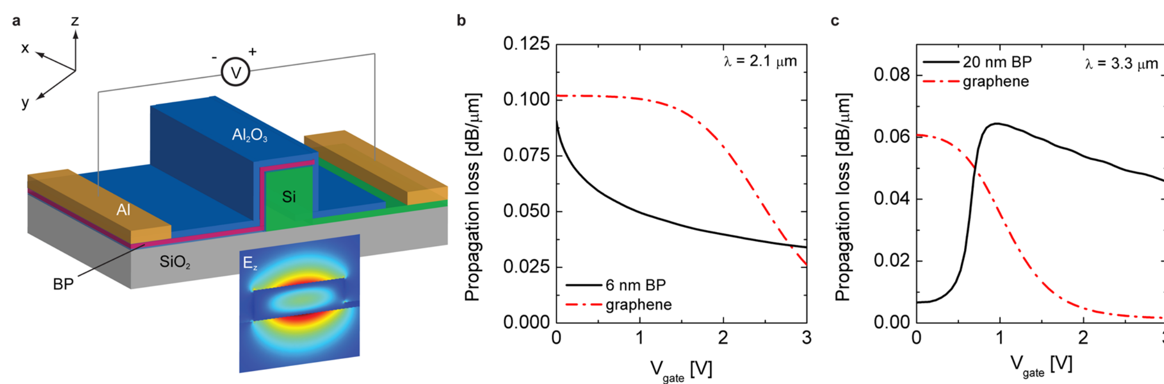

Figure 4. (a) Schematic of BP-assisted, traveling-wave electro-absorption modulator. The Si waveguide is connected to a partially etched, 50 nm-thick Si layer that serves as a contact electrode. The Si layer is assumed to be undoped in optical simulation. The waveguide is encapsulated by a 50 nm Al_2O_3 passivation layer. The effective numerical thickness of BP is taken to be 0.7 nm.[26] The transverse-magnetic mode profile is shown in inset. (b) Waveguide loss for modulator integrated with 6 nm BP active layer, operating at $\lambda = 2.1$ μm. The thickness and width of the Si core are 310 and 1000 nm, respectively. The performance of the modulator where BP is replaced with monolayer graphene is displayed for comparison. (c) Waveguide loss for modulator integrated with 20 nm BP active layer, operating at $\lambda = 3.3$ μm. The thickness and width of the Si core are 500 and 1340 nm, respectively.

the magnitude of σ_{xx} increases with BP thickness. For low N_s, the optical band edge shifts toward lower energy and follows closely with E_g. The shift is more abrupt for thicker QW due to stronger QCFK effect. For higher N_s, the band edge deviates from E_g and shift toward higher energy due to BMS. The shift is more abrupt for thinner film due to more rapid band filling, since the subbands are more apart in energy.

Note that, for BP films thinner than those studied in this paper, bandgap renormalization and strong excitonic effects are also expected due to reduced screening.[23,41,46] This may lead to further band edge shift and enhanced light absorption not accounted for in present calculations.

For proof-of-concept, we study the performance of a simple modulator design, consisting of BP thin film overlaid on top of a Si nanowire, separated by a 7 nm Al_2O_3 spacer (Figure 4a). To avoid the degradation of BP in ambient,[47] we have also added a 50 nm Al_2O_3 passivation layer[48] in our device structure. To maximize the overlap between the optical mode and the actively modulated BP layer, the transverse-magnetic mode (Figure 4a, inset) is chosen for modulation and BP's crystal axes in the amrchair direction is assumed to align with the direction of light propagation. Such modulator configuration was reported in the initial demonstration of graphene-assisted modulator.[26]

Figure 4b shows the static electro-optical modulator response using BMS-dominant, 6 nm BP thin film, operating at $\lambda = 2.1$ μm. For comparison, the modulator response with multilayer BP replaced by monolayer graphene is also displayed (see Supplementary Figure S2 for graphene's optical conductivity model).[49] Due to their semimetallic and semiconducting nature, BP has a vertical electric field screening length of order of 10 nm,[50] thereby allowing multilayer BP to be used for modulation. Contrarily, the screening length of multilayer graphene was of order of the interlayer spacing,[51] thus preventing such system from being utilized for modulation. However, while the waveguide loss associated with 6 nm BP is more sensitive to bias at lower gate voltage (V_{gate}), monolayer graphene enables more rapid decay at higher V_{gate}. This is a consequence of the quenching of the BMS effect due to the QCFK mechanism.

Conversely, by increasing BP layer thickness, the V_{gate} required to induce the onset of BMS increases, thereby allowing stronger QCFK effect to manifest. Figure 4c shows the response of a 20 nm BP-assisted modulator, operating at $\lambda = 3.3$ μm. Recent experiment have shown low-loss light propagation through SOI platform near 3 μm, showing promise for integrated MIR data communication.[52] Here, the waveguide loss increases and decreases for V_{gate} below and above 0.89 V,

DOI: 10.1021/acs.nanolett.5b04594
Nano Lett. 2016, 16, 1683–1689

respectively, indicating a transition between the QCFK and BMS regimes. The change in waveguide loss is more rapid in the QCFK regime, since the modulation is via an effective change in transition energy gap, below which there are no available electronic density of states for the optical transition. Conversely, BMS relies on Pauli blocking, where the optical transition edge is smeared in energy by kT. Operating in the QCFK regime, the performance of 20 nm BP compares favorably against graphene: (1) The maximal attainable absorption is 0.65 and 0.61 dB/μm for BP and graphene, respectively. (2) Defining the modulator power consumption (P) as the voltage swing required to reduce the waveguide loss from maximally lossy state (OFF-state) to 0.01 dB/μm (ON-state), BP-assisted modulator only requires P = 0.59 V. This is a 62% reduction compared to the use of BMS effect in its graphene counterpart (P = 1.56 V).

One popular figure-of-merit (FOM) for optical modulators is the ratio of extinction ratio over insertion loss, where extinction ratio is the difference between the ON-state and the OFF-state losses while insertion loss is the ON-state loss.[53] Although QCFK is quenched by BMS in the current modulator design, the device achieves a FOM of 5.5 and uses only a single BP QW that couple evanescently with the optical mode. This exceeds the FOM = 1.6−4 as obtained with QCSE-based SiGe modulators,[53] which places multiple (>10) QWs in a carrier-depleted PIN junction as a crystalline, multilayer waveguide core. Thus, layering of BP with other 2D materials to engineer analogous heterojunctions may further enhance the performance of BP-assisted modulators.

In summary, we demonstrated the versatility of BP's electro-absorption characteristics in the MIR. Controlled by the interplay of QCFK and BMS effects, the optical bandgap may undergo blue-shift, red-shift, or bidirectional-shift for a given doping range, film thickness, and wavelength. This is afforded by the reduced dimensionality and finite bandgap of BP, which departs from the unidirectional shift observed in graphene and traditional III−V semiconductors. The simulation of a simple modulator design indicates that QCFK effect is superior than BMS as an electro-absorption mechanism in BP thin-films. Operating in QCFK regime leads to enhanced maximal attainable absorption and reduced power consumption compared to its graphene counterpart. Overall, the gate-tunable optical characteristics make multilayer BP an attractive, alternative material platform for integrated optoelectronic systems in the MIR.

Methods. *Optical Conductivity Model of Multilayer Black Phosphorus.* Based on $k{\cdot}p$ theory and symmetry arguments, the in-plane, low-energy Hamiltonian around the Γ point can be described as[37]

$$H = \begin{pmatrix} E_c + \eta_c k_x^2 + \nu_c k_y^2 & \gamma k_x \\ \gamma k_x & E_v - \eta_v k_x^2 - \nu_v k_y^2 \end{pmatrix} \tag{4}$$

where E_c and E_v are the energies of the conduction and valence band edges, while γ describes the effective couplings between the two bands. The $\eta_{c,v}$ and $\nu_{c,v}$ terms are related to the in-plane effective masses, given by $m_{cx} = \hbar^2/[2\gamma^2/(E_c - E_v) + \eta_c]$ and $m_{cy} = \hbar^2/2\nu_c$ for electrons. They are chosen such that they yield the known effective masses in the bulk limit ($m_{cx} = m_{vx} = 0.08m_0$, $m_{cy} = 0.7m_0$, and $m_{vy} = 1.0m_0$)[17,34] and monolayer BP ($m_{cx} = m_{vx} \approx 0.15m_0$, $m_{cy} \approx 0.7m_0$, and $m_{vy} \approx 1.0m_0$).[37] Analogous expression applies for the hole case. Using known anisotropic effective masses for monolayer and bulk BP films,[17,19,34] we set: $\eta_{c,v} = \hbar^2/0.4m_0$, $\nu_c = \hbar^2/1.4m_0$, $\nu_v = \hbar^2/2.0m_0$, and $\gamma = 4a/\pi$ eV m. The value of β is taken to be $2a^2/\pi^2$ eV/m^2, where a = 2.23 Å and π/a is the width of the BZ in the x direction.

Due to quantum confinement, $E_{c,v}$ in eq 4 needs to be replaced with $E^j_{c,v}$, where j denotes the subband number. Moreover, additional confinement energies ($\delta_{c,v}(t_z)$) are incorporated in our model to reproduce the predicted energy gap of the BP film, of 2 and 0.3 eV in the monolayer and bulk limit, respectively.[19,23] For electrons, they are given by $\delta E^j_c = j^2\hbar^2\pi^2/2m_{cz}t_z + \delta_{c,v}(t_z)$, where t_z is the thickness of the BP film, and $m_{cz} \approx 0.2\ m_0$ is the electron effective mass along the z direction.[19,34] Analogous expression applies for the hole case ($m_{vz} \approx 0.4\ m_0$).

The subband energies can be obtained through self-consistent the solution of the Schrödinger-Poisson equations:[38]

$$\frac{d^2\varphi(z)}{dz^2} = \frac{-4\pi e^2}{\epsilon_{BP}} \times \sum_j \left[\frac{m^j_{DOS} k_B T}{\pi\hbar^2} \ln\left(1 + \exp\left(\frac{E_f - E^j_c}{k_B T}\right)\right) |\psi(z)^2| \right] \tag{5}$$

where E_f is the Fermi level, $m^j_{DOS} = (m^j_{cx} m^j_{cy})^{1/2}$ is the subband density-of-states mass, and ϵ_{BP} = 8.3 is the out-of-plane dielectric constant of BP.[17]

Finally, the optical conductivity of BP can be evaluated via the Kubo formula:

$$\sigma_{\alpha\beta}(\mathbf{q}, \omega) = -i\frac{g_s h e^2}{(2\pi)^2} \sum_{ss'jj'} \int d\mathbf{k} \frac{f(E_{sj\mathbf{k}}) - f(E_{s'j'\mathbf{k}'})}{E_{sj\mathbf{k}} - E_{s'j'\mathbf{k}'}} \times \frac{\langle \Phi_{sj\mathbf{k}} | \hat{\nu}_\alpha | \Phi_{s'j'\mathbf{k}'} \rangle \langle \Phi_{s'j'\mathbf{k}'} | \hat{\nu}_\beta | \Phi_{sj\mathbf{k}} \rangle}{E_{sj\mathbf{k}} - E_{s'j'\mathbf{k}'} + \hbar\omega + i\eta} \tag{6}$$

where $\hat{\nu}_\alpha$ is the velocity operator defined as $\hbar^{-1}\delta_{k\alpha}H$, g_s = 2 accounts for the spin degeneracy, and η is a phenomenological broadening term to account for finite damping, assigned to be 5 meV. E_{sjk} and Φ_{sjk} are the eigenenergies and eigenfunctions of H. $f(...)$ is the Fermi−Dirac distribution function. The indices $\{s,s\} = \pm 1$ denotes a conduction/valence band.

The dielectric constant of BP (ϵ) can subsequently be calculated via:

$$\epsilon = 1 - \frac{\sigma}{j\omega\epsilon_0\Delta} \tag{7}$$

where ϵ_0 is the vacuum permittivity and Δ = 0.7 nm is used as the numerical effective thickness of BP.[26]

Optical Simulation Setup. The propagation loss of the optical mode was calculated via two-dimensional finite element method simulation using commercial Lumerical Mode Solutions software. Metallic boundary conditions were utilized to terminate the 2 μm × 2 μm computational domain. Grid sizes of 0.1, 1, and 2.5 nm were used to mesh the BP thin film, the Al_2O_3 spacer layer, and the rest of the waveguide structure, respectively.

The 50 nm thick Si layer that serves as the contact to the Si bus waveguide is taken to be intrinsic in the simulations. The refractive indices of the materials at λ = 2.1 μm (3.3 μm) were as follows: n_{Si} = 3.45 (3.43), n_{SiO2} = 1.44 (1.41), and n_{Al2O3} = 1.74 (1.7).

DOI: 10.1021/acs.nanolett.5b04594
Nano Lett. 2016, 16, 1683−1689

Gate Voltage Calculation. Using a capacitor model, the carrier concentration (N_s) in BP thin films can be related to applied gate voltage (V_{gate}) via the following expression:

$$V_{gate} = V_{fb} + E_f - E_c(z = 0) + \frac{q_0 N_s}{\epsilon_0 \epsilon_{ox}} t_{ox} \quad (8)$$

where $V_{fb} = 0$ V is the flat band voltage, E_f is the Fermi energy, E_c is the BP conduction band energy, t_{ox} is the spacer layer thickness, q_0 is the fundamental charge, and ϵ_0 and ϵ_{ox} are the permittivity of free space and spacer layer, respectively.

■ ASSOCIATED CONTENT

Supporting Information

The Supporting Information is available free of charge on the ACS Publications website at DOI: 10.1021/acs.nanolett.5b04594.

Details of the imaginary part of BP's optical conductivity and graphene's optical model (PDF)

■ AUTHOR INFORMATION

Corresponding Author

*E-mail: charleschihchin.lin@mail.utoronto.ca.

Notes

The authors declare no competing financial interest.

■ REFERENCES

(1) Soref, R. *Nat. Photonics* **2010**, *4*, 495−497.
(2) Stanley, R. *Nat. Photonics* **2012**, *6*, 409−411.
(3) Swiderski, J. *Prog. Quantum Electron.* **2014**, *38*, 189−235.
(4) Schliesser, A.; Picque, N.; Hansch, T. W. *Nat. Photonics* **2012**, *6*, 440−449.
(5) Singh, V.; Lin, P. T.; Patel, N.; Lin, H.; Li, L.; Zou, Y.; Deng, F.; Ni, C.; Hu, J.; Giammarco, J. *Sci. Technol. Adv. Mater.* **2014**, *15*, 014603.
(6) Miller, D. A. B.; Chemla, D. S.; Damen, T. C. *Phys. Rev. Lett.* **1984**, *53*, 2173−2176.
(7) Kuo, Y.-H.; Lee, Y. K.; Ge, Y.; Ren, S.; Roth, J. E.; Kamins, T. I.; Miller, D. A. B.; Harris, J. S. *IEEE J. Sel. Top. Quantum Electron.* **2006**, *12*, 1503−1513.
(8) Kuo, Y.-H.; Lee, Y. K.; Ge, Y.; Ren, S.; Roth, J. E.; Kamins, T. I.; Miller, D. A. B.; Harris, J. S. *Nature* **2005**, *437*, 1334−1336.
(9) Arad, U.; Redmard, E.; Shamay, M.; Averboukh, A.; Levit, S.; Efron, U. *IEEE Photonics Technol. Lett.* **2003**, *15*, 1531−1533.
(10) Liu, C. P.; Seeds, A.; Chadha, J. S.; Stavrinou, P. N.; Parry, G.; Whitehead, M.; Krysa, A. B. *IEICE Trans. Electron. E* **2003**, *86C*, 1281−1289.
(11) Liu, J.; Beals, M.; Pomerene, A.; Bernardis, S.; Sun, R.; Cheng, J.; Kimerling, L. C.; Michel, J. *Nat. Photonics* **2008**, *2*, 433−437.
(12) Kim, Y.; Takenaka, M.; Osada, T.; Hata, M.; Takagi, S. *Sci. Rep.* **2014**, *4*, 4683.
(13) Li, L.; Yu, Y.; Ye, G. J.; Ge, Q.; Ou, X.; Wu, H.; Feng, D.; Chen, X. H.; Zhang, Y. *Nat. Nanotechnol.* **2014**, *9*, 372−377.
(14) Liu, H.; Neal, A. T.; Zhu, Z.; Tomanek, D.; Ye, P. D. *ACS Nano* **2014**, *8*, 4033−4041.
(15) Xia, F.; Wang, H.; Jia, Y. *Nat. Commun.* **2014**, *5*, 4458.
(16) Koenig, S. P.; Doganov, R. A.; Schmidt, H.; Neto, A. H.; Ozyilmaz, B. *Appl. Phys. Lett.* **2014**, *104*, 103106.
(17) Morita, A. *Appl. Phys. A: Solids Surf.* **1986**, *39*, 227−242.
(18) Buscema, M.; Groenendijk, D. J.; Blanter, S. I.; Steele, G. A.; van der Zant, H. S. J.; Castellanos-Gomez, A. *Nano Lett.* **2014**, *14*, 3347−3352.
(19) Low, T.; Engel, M.; Steiner, M.; Avouris, P. *Phys. Rev. B: Condens. Matter Mater. Phys.* **2014**, *90*, 081408.
(20) Low, T.; Rodin, A. S.; Carvalho, A.; Jiang, Y.; Wang, H.; Xia, F.; Castro Neto, A. H. *Phys. Rev. B: Condens. Matter Mater. Phys.* **2014**, *90*, 075434.
(21) Qiao, J.; Kong, X.; Hu, Z. X.; Yang, F.; Ji, W. *Nat. Commun.* **2014**, *5*, 4475.
(22) Andres, C. G.; Vicarelli, L.; Prada, E.; Island, J. O.; Narasimha-Acharya, K. L.; Blanter, S. I.; Groenendijk, D. J.; Buscema, M.; Steele, G. A.; Alvarez, J. V.; Zandbergen, H. W.; Palacios, J. J.; van der Zant, H. S. J. *2D Mater.* **2014**, *1*, 025001.
(23) Tran, V.; Soklaski, R.; Liang, Y.; Yang, L. *Phys. Rev. B: Condens. Matter Mater. Phys.* **2014**, *89*, 235319.
(24) Moss, T. S. *Proc. Phys. Soc., London, Sect. B* **1954**, *67*, 775−782.
(25) Burstein, E. *Phys. Rev.* **1954**, *93*, 632−633.
(26) Liu, M.; Yin, X.; Ulin-Avila, E.; Geng, B.; Zentgraf, T.; Ju, L.; Wang, F.; Zhang, X. *Nature* **2011**, *474*, 64−67.
(27) Lu, S. B.; Miao, L. L.; Guo, Z. N.; Qi, X.; Zhao, C. J.; Zhang, H.; Wen, S. C.; Tang, D. Y.; Fan, D. Y. *Opt. Express* **2015**, *23*, 11183−11194.
(28) Guo, Z.; Zhang, H.; Lu, S.; Wang, Z.; Tang, S.; Shao, J.; Sun, Z.; Xie, H.; Wang, H.; Yu, X. F.; Chu, P. K. *Adv. Funct. Mater.* **2015**, *25*, 6996−7002.
(29) Engel, M.; Steiner, M.; Avouris, P. *Nano Lett.* **2014**, *14*, 6414−6417.
(30) Youngblood, N.; Chen, C.; Koester, S. J.; Li, M. *Nat. Photonics* **2015**, *9*, 247−252.
(31) Rudenko, A. N.; Katsnelson, M. I. *Phys. Rev. B: Condens. Matter Mater. Phys.* **2014**, *89*, 201408.
(32) Wu, R. J.; Topsakal, M.; Low, T.; Robbins, M. C.; Haratipour, N.; Jeong, J. S.; Wentzcovitch, R. M.; Koester, S. J.; Mkhoyan, K. A. *J. Vac. Sci. Technol., A* **2015**, *33*, 060604.
(33) Cakir, D.; Sevik, C.; Peeters, F. M. *Phys. Rev. B: Condens. Matter Mater. Phys.* **2015**, *92*, 165406.
(34) Narita, S.; Terada, S.; Mori, S.; Muro, K.; Akahama, Y.; Endo, S. *J. Phys. Soc. Jpn.* **1983**, *52*, 3544−3553.
(35) Mattheiss, L. F. *Phys. Rev. B* **1973**, *8*, 3719.
(36) Wallace, P. R. *Phys. Rev.* **1947**, *71*, 622.
(37) Rodin, A. S.; Carvalho, A.; Castro Neto, A. H. *Phys. Rev. Lett.* **2014**, *112*, 176801.
(38) Stern, F. *J. Comput. Phys.* **1970**, *6*, 56−67.
(39) Kim, J.; Baik, S. S.; Ryu, S. H.; Sohn, Y.; Park, S.; Park, B.; Denlinger, J.; Yi, Y.; Choi, H. J.; Kim, K. S. *Science* **2015**, *349*, 723.
(40) Miller, D. A. B.; Chemla, D. S.; Schmitt-Rink, S. *Phys. Rev. B: Condens. Matter Mater. Phys.* **1986**, *33*, 6976.
(41) Chaves, A.; Low, T.; Avouris, P.; Cakir, D.; Peeters, F. M. *Phys. Rev. B: Condens. Matter Mater. Phys.* **2015**, *91*, 155311.
(42) Wang, F.; Zhang, Y.; Tian, C.; Girit, C.; Zettl, A.; Crommie, M.; Shen, Y. R. *Science* **2008**, *320*, 206−209.
(43) Li, Z. Q.; Henriksen, E. A.; Jiang, Z.; Hao, Z.; Martin, M. C.; Kim, P.; Stormer, H. L.; Basov, D. N. *Nat. Phys.* **2008**, *4*, 532−535.
(44) Nair, R. R.; Blake, P.; Grigorenko, A. N.; Novoselov, K. S.; Booth, T. J.; Stauber, T.; Peres, N. M. R.; Geim, A. K. *Science* **2008**, *320*, 1308.
(45) Mak, K. F.; Sfeir, M. Y.; Wu, Y.; Lui, C. H.; Misewich, J. A.; Heinz, T. F. *Phys. Rev. Lett.* **2008**, *101*, 196405.
(46) Wang, X.; Jones, A. M.; Seyler, K. L.; Tran, V.; Jia, Y.; Zhao, H.; Wang, H.; Yang, L.; Xu, X.; Xia, F. *Nat. Nanotechnol.* **2015**, *10*, 517−521.
(47) Favron, A.; Gaufres, E.; Fossard, F.; Phaneuf-L'Heureux, A.-L.; Tang, N. Y.-W.; Levesque, P. L.; Loiseau, A.; Leonelli, R.; Francoeur, S.; Martel, R. *Nat. Mater.* **2015**, *14*, 826−832.
(48) Wood, J. D.; Wells, S. A.; Jariwala, D.; Chen, K.-S.; Cho, E. K.; Sangwan, V. K.; Liu, X.; Lauhon, L. J.; Marks, T. J.; Hersam, M. C. *Nano Lett.* **2014**, *14*, 6964−6970.
(49) Falkovsky, L. A.; Varlamov, A. A. *Eur. Phys. J. B* **2007**, *56*, 281−284.
(50) Low, T.; Roldan, R.; Wang, H.; Xia, F.; Avouris, P.; Moreno, L. M.; Guinea, F. *Phys. Rev. Lett.* **2014**, *113*, 106802.
(51) Kuroda, M. A.; Tersoff, J.; Martyna, G. J. *Phys. Rev. Lett.* **2011**, *106*, 116804.

DOI: 10.1021/acs.nanolett.5b04594
Nano Lett. 2016, 16, 1683−1689

(52) Mashanovich, G. Z.; Milosevic, M. M.; Nedeljkovic, M.; Owens, N.; Xiong, B.; Teo, E. J.; Hu, Y. *Opt. Express* **2011**, *19*, 7112−7119.
(53) Schaevitz, R. K.; Edwards, E. H.; Roth, J. E.; Fei, E. T.; Rong, Y.; Wahl, P.; Kamins, T. I.; Harris, J. S.; Miller, D. A. B. *IEEE J. Quantum Electron.* **2012**, *48*, 187−197.

DOI: 10.1021/acs.nanolett.5b04594
Nano Lett. 2016, 16, 1683−1689